Fuel 393 (2025) 134931

Contents lists available at ScienceDirect

Fuel

journal homepage: www.elsevier.com/locate/fuel

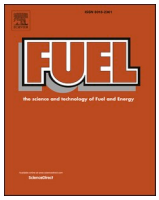

Full Length Article

Enhanced performance of Cu-based perovskite catalyst for CO_2 hydrogenation to methanol

Yuxin Shi, Lingjun Zhu *, Jiaqi Tang, Kunzan Qiu, Shurong Wang *

State Key Laboratory of Clean Energy Utilization, Zhejiang University, Hangzhou 310027, China

ARTICLE INFO

Keywords:
CO_2 hydrogenation
Methanol synthesis
Perovskite catalyst
Citrate complexation method
La_2CuO_4

ABSTRACT

The direct catalytic synthesis of methanol from CO_2 and H_2 has emerged as a significant area of research for the high-value utilization of CO_2. Cu-based catalysts have attracted considerable attention due to their cost-effectiveness and superior performance. In this study, we developed a novel catalyst, LMCZ-181, derived from the perovskite-type precursor La_2CuO_4 through a citrate complexation method. The findings revealed that doping with Mn and Zn modified the catalyst's crystal structure by increasing oxygen vacancies and promoting the formation of active sites, consequently enhancing catalytic activity. The results of In-situ DRIFTS demonstrated that these catalysts facilitated CO_2 hydrogenation via the formate pathway and confirmed that LMCZ-181 possessed superior hydrogenation capability. At an operating temperature of 270°C, LMCZ-181 exhibited optimal catalytic activity and stability, achieving a CO_2 conversion of 20.81 % and a methanol selectivity of 77.68 %. This study provides an effective strategy for developing highly active and stable catalysts for CO_2 hydrogenation for methanol production.

1. Introduction

The combustion of fossil fuels and CO_2 emissions from various human activities are recognized as the primary contributors to global warming. In 2020, the International Energy Agency proposed that achieving net-zero global energy-related CO_2 emissions by 2050 could limit the increase in global temperature to within 1.5 °C [1]. Consequently, addressing the current dilemma has emerged as one of the urgent challenges that each nation must confront. As a carbon resource in critical demand for development, CO_2 can be recycled through the production of chemicals, materials, and fuels to mitigate its emissions. Thus, the issue of CO_2 utilization has garnered significant attention globally.

With the Carbon Capture, Utilization, and Storage (CCUS) technology, CO_2 is captured and refined during its production; and it is subsequently used as a raw material in other manufacturing processes [2]. This technology not only stores CO_2; but also enables the resource and energy utilization of CO_2. Among these, the direct catalytic synthesis of methanol from CO_2 and H_2 is regarded as a pivotal technology for mitigating CO_2 emissions with promising development prospects.

Methanol serves as both a crucial chemical raw material and a clean fuel that is easy to store and transport. It is widely regarded as an alternative to conventional fossil fuels, leading to an increasing demand in the industry [3]. Relative to other organic fuels, methanol presents several advantages, including a low boiling point, more efficient combustion, ease of production, and reduced emissions of CO and NO_x. Moreover, methanol can be utilized for the production of high-value petrochemical products, such as olefins, aromatics, and gasoline. The technology for synthesizing methanol via CO_2 hydrogenation not only addresses environmental challenges, including the greenhouse effect; but also enhances the utilization of carbon resources. This technology is considered one of the most effective means for mitigating global warming and advancing the chemical industry [4].

The CO_2 hydrogenation process to produce methanol involves two primary reactions: the synthesis of methanol and the reverse water gas shift reaction (RWGS):

$$CO_2 + 3H_2 \rightleftharpoons CH_3OH + H_2O \ \Delta H = \text{-}49.5 \text{ kJ/mol} \quad (1)$$

$$CO_2 + H_2 \rightleftharpoons CO + H_2O \ \Delta H = 41.2 \text{ kJ/mol} \quad (2)$$

The methanol synthesis reaction is exothermic, while the RWGS is endothermic [5], consequently, the conversion rate of CO_2 decreases with increasing reaction temperature. Although elevated temperatures facilitate CO_2 activation, they can negatively impact the selectivity for

* Corresponding authors.
E-mail addresses: lingjun_zhu@zju.edu.cn (L. Zhu), srwang@zju.edu.cn (S. Wang).

https://doi.org/10.1016/j.fuel.2025.134931
Received 22 January 2025; Received in revised form 27 February 2025; Accepted 2 March 2025

methanol. Therefore, the synthesis of methanol from CO_2 is limited by thermal equilibrium, necessitating the development of a catalyst that operates effectively at an optimal temperature to enhance catalytic performance [6,7]. Additionally, the water generated during the reaction can lead to the sintering of active sites on the catalyst, resulting in catalyst deactivation [8]. To sum up, the exploration of suitable promoters supports, and catalyst structures is crucial for enhancing both the catalytic efficiency and stability of the catalyst.

Currently, the prevalent catalysts for converting CO_2 to methanol include Cu-based catalysts, precious metal catalysts, bimetallic catalysts, and composite oxide catalysts. Among these, Cu-based catalysts stand out due to their cost-effectiveness and enhanced industrial production efficiency, making them the preferred choice for CO_2-to-methanol conversion. However, Cu-based catalysts can also facilitate the RWGS and methanol decomposition reaction [9], which inevitably results in the formation of byproduct CO during methanol synthesis from CO_2. Substantial efforts have been invested in refining Cu-based catalysts to enhance methanol selectivity. Dong et al. [10] developed a series of Cu/ZnO/ZrO_2 catalysts utilizing a precipitation-reduction method, which exhibited significantly improved methanol selectivity compared to those prepared by conventional precipitation techniques. At 270 °C, this catalyst achieved a CO_2 conversion of 23 % and a methanol selectivity of 56.8 %. Wu et al. [11] synthesized a reverse ZrO_2/Cu catalyst with an adjustable zirconium-to-copper ratio through an oxalate co-precipitation method, demonstrating promising performance in CO_2 hydrogenation to methanol. Guo et al. [12] prepared a series of Cu/ZrO_2 catalysts with varying La loadings; under conditions of 220 °C and 5 MPa, the methanol selectivity of these catalysts increased from 58 mol% to 72 mol% with an elevated La content. Yao et al. [13] synthesized a series of Cu-In-Zr-O composite oxide nanomaterials featuring defective In_2O_3 active centers. Compared to In-Zr-O catalysts, Cu-In-Zr-O catalysts exhibited superior CO_2 conversion rates and methanol selectivity, highlighting the synergistic effect between the Cu and In_2O_3 active centers.

In recent years, perovskite oxides have garnered significant attention due to their high activity and stability [14,15]. The general formula for perovskite oxides is ABO_3 or A_2BO_4. The A site is occupied by the larger rare earth or alkaline earth metal cation, while the B site is occupied by smaller transition metal cations capable of forming octahedral coordination with six oxygen ions. The A site provides structural integrity in these structures, while the B site supplies active catalytic sites. By reducing the metal cations located at the B site, high dispersion of metal elements can be achieved, rendering perovskite-type oxides ideal precursors for catalysts [16,17]. The distinctive structure of perovskite oxides facilitates the fine dispersion of "metal oxides" through reduction, attracting considerable interest in the field of catalysis [18]. Maluf et al. [19] prepared $La_{2-x}M_xCuO_4$ perovskites (where M = Ce, Ca, or Sr) as catalysts for the water–gas shift reaction and evaluated their performance at 290 °C and 360 °C. Among these, $La_{2-x}Ce_xCuO_4$ demonstrated the highest catalytic performance, achieving a CO conversion of 85–90 %. Zhang et al. [20] prepared composite metal oxide $(La_2CuO_4)_x$(CNZ-1)$_{1-x}$ (x = 0.3, 0.5, 0.7) as nano-catalysts for methanol steam reforming reaction studies. The results indicated that the LCO$_x$-CNZ catalyst exhibited higher methanol conversion and hydrogen yield compared to the La_2CuO_4 catalyst. In contrast, perovskites have garnered less attention in methanol synthesis research. The catalytic reaction conditions in these studies are relatively harsh, and the types and contents of metals in perovskites still need to be adjusted to enhance their catalytic activity. Mahomed et al. [21] explored the influence of La doping on the catalytic activity of Cu-CeO_2 in the hydrogenation of CO_2 to methanol. The incorporation of La facilitated the formation of smaller CeO_2 crystallites within the catalyst, thereby increasing the number of active sites and enhancing catalytic activity. Wei et al. [22] synthesized a series of La-M-Cu-Zn-O (M = Y, Ce, Mg, Zr) catalysts with a perovskite structure using the sol–gel method. At 250 °C and 5.0 MPa, CO_2 conversion and methanol selectivity achieved 12.6 % and 52.5 %, respectively.

To investigate the catalytic effects of Cu-based perovskite catalysts in the hydrogenation of CO_2 to methanol, this study employed a citric acid salt complexation method to synthesize three types of Cu-based perovskite catalysts with the following molar stoichiometries: $LaCuO_3$, $LaCu_{0.8}Zn_{0.2}O_3$, and $LaMn_{0.1}Cu_{0.8}Zn_{0.1}O_3$. Performance testing and characterization analysis were performed on these catalysts to evaluate their effectiveness. Furthermore, the influence of Mn and Zn doping on both the perovskite structure and catalytic performance was investigated. The physicochemical properties and the structure–activity relationships of the catalysts were comprehensively analyzed and discussed.

2. Experimental section

2.1. Catalysts preparation

The perovskite oxides, including $LaCuO_3$, $LaCu_{0.8}Zn_{0.2}O_3$, and $LaMn_{0.1}Cu_{0.8}Zn_{0.1}O_3$, were synthesized using the citrate complexation method with citric acid as a complexing agent. A sufficient quantity of precursor salts, including $La(NO_3)_3{\cdot}6H_2O$, $Cu(NO_3)_2{\cdot}3H_2O$, $Zn(NO_3)_2{\cdot}6H_2O$, $Mn(NO_3)_2$, were combined with citric acid and ethylene glycol in a molar ratio of 2: 1: 4 (all metal cations: citric acid: ethylene glycol = 2: 1: 4), and dissolved in deionized water to create a homogeneous solution. In these compounds, the molar ratios of La to Cu are 1: 1 in $LaCuO_3$; the metal element ratios of La: Cu: Zn are 1: 0.8: 0.2 in $LaCu_{0.8}Zn_{0.2}O_3$; and the metal element ratios of La: Mn: Cu: Zn are 1: 0.1: 0.8: 0.1 in $LaMn_{0.1}Cu_{0.8}Zn_{0.1}O_3$. The solution was stirred overnight at room temperature and subjected to microwave heating at 80 °C for 1 h to facilitate the formation of the complex. Subsequently, it was heated in an oil bath at 90 °C to remove water. After forming a blue-green, honey-like gel, the mixture was transferred to a drying oven for drying at 100 °C. Finally, the dried gel was calcined at 300 °C for 2 h, followed by an increase in temperature to 700 °C for 3 h. The catalysts obtained after calcination were labeled LC, LCZ-82, and LMCZ-181. To differentiate between catalysts following calcination, reduction, and utilization, labels C, R, and U are assigned individually.

2.2. Catalysts characterization

The X-ray diffraction (XRD) analysis was performed using the PANalytical X'Pert3 Powder-17005730 X-ray diffractometer. This instrument operated with Cu Kα radiation as the X-ray source, under the conditions of 40 kV and 40 mA. The diffraction angle 2θ spanned from 10° to 90°, with a fixed step size of 0.026° and a data acquisition time of 30 s. XRD enabled the determination of the active components' phase composition and lattice parameters within the catalyst, along with the calculation of copper grain size using the Scherrer formula [23]. Jade software was used to perform phase identification on the diffraction peak data to obtain grain size and calculate the lattice constants through cell refinement based on the least squares method.

The structural properties of the porous materials were characterized by conducting N_2 adsorption–desorption tests using the Quantachrome ASiQwin instrument. The specific surface area of the catalysts was determined by the Brunauer-Emmett-Teller (BET) method.

The hydrogen temperature programmed reduction (H_2-TPR) test was conducted using the BELCAT-B equipment. Initially, a specific quantity of sample was loaded into the reactor, and inert gas was introduced to raise the temperature to 300 °C for 30 min of pretreatment. Subsequently, the temperature was reduced to 100 °C, and inert gas flowed at this temperature until the baseline stabilized. Finally, a mixture of 10 % H_2/Ar gas was introduced while gradually increasing the temperature at 10 °C/min until reaching 700 °C. The consumption of H_2 during this experiment was monitored using a thermal conductivity detector (TCD).

A similar procedure was employed for the hydrogen temperature programmed desorption (H_2-TPD) test on the same BELCAT-B instrument to gather information about the active catalytic sites. The catalyst

underwent a reduction in 10 % H_2/Ar with a flow rate of 30 mL/min at 300 °C for 2 h. After cooling to ambient temperature, it was saturated with pure H_2 at 100 °C for 1 h. After this, the sample was purged with inert gas at the adsorption temperature until a stable baseline was achieved. The experimental apparatus was then heated to 900 °C at a rate of 10 °C/min to initiate the TPD experiment, during which a TCD monitors variations in the hydrogen signal.

The CO_2 temperature programmed desorption (CO_2-TPD) test was performed under the same conditions used for the H_2-TPD test, over a temperature range of 100 °C to 700 °C. CO_2-TPD assessed the qualitative analysis of the quantity and strength of basic sites in the catalyst. Before testing, samples were pretreated at 300 °C for 60 min in 10 % H_2/Ar, then cooled to 100 °C. Subsequently, CO_2 was introduced and maintained for 30 min to ensure sufficient CO_2 adsorption. Finally, residual CO_2 was purged using an inert gas while concentration changes were recorded via TCD during the subsequent desorption process.

The morphology of the samples was analyzed using a SU-8010 scanning electron microscope (SEM) operated at an accelerating voltage of 3.0 kV. The SEM was coupled with an Oxford X-max80 energy dispersive spectrometer, enabling a preliminary quantitative analysis of the uniformity of elemental distribution within the catalyst and the ratios of each element. Transmission electron microscopy (TEM) was conducted using an FEI Tecnai F20 transmission electron microscope to observe and analyze the active components present on the catalyst surface. Additionally, high-resolution TEM (HRTEM) revealed the detailed lattice structure of the perovskite catalyst.

The samples were analyzed using the Thermo Scientific K-alpha instrument for X-ray photoelectron spectroscopy (XPS). The excitation source used Al Kα radiation (hv = 1486.6 eV) at an operating voltage of 12 kV and a filament current of 6 mA. Signals were accumulated over 10 cycles. The full spectrum pass energy was set at 150 eV, with a step size of 1 eV and a dwell time of 40–50 ms. The data were charge-corrected by referencing the C1s binding energy at 284.80 eV as the energy standard.

To elucidate the catalytic reaction mechanism of CO_2 hydrogenation to methanol, in-situ Diffuse Reflectance Infrared Fourier Transform Spectroscopy (DRIFTS) was employed to characterize surface-adsorbed intermediates and the reaction pathway of the catalysts. Initially, the samples were reduced by heating to 300 °C under a 10 % H_2/N_2 atmosphere (30 mL/min) for 2 h, followed by cooling to room temperature. The gas flow was subsequently switched to pure N_2 and purged for 30 min to record the background spectrum. A CO_2:H_2 mixture with a ratio of 1:3 (30 mL/min) was introduced into the reaction chamber, and spectra were collected at 210 °C and 270 °C.

2.3. Evaluation of catalysts performance

The performance tests of Cu-based catalysts were conducted using an eight-channel catalyst evaluation system (MPRS-8TS). This fixed-bed reactor comprises eight stainless steel tubes, each with an inner diameter of 8 mm, and the reaction pressure was regulated by a pressure control valve. Prior to the experiment, 1 g of catalyst with a particle size of 60–80 mesh was positioned in the constant temperature zone in the middle of the reaction tube. Before initiating the test, the catalyst was reduced in an H_2 atmosphere at a flow rate of 50 mL/min for 3 h at 350 °C. When the catalyst temperature decreased to 150 °C, the reaction pressure was adjusted to 3 MPa, and the temperature was gradually increased to the initial reaction temperature of 210 °C at a heating rate of 5 °C/min. Within the reactor, a gas mixture containing CO_2, H_2, and N_2 was introduced in a ratio of CO_2: H_2: N_2 = 8: 24: 1. The gas-hour space velocity of each channel was 6000 $mL{\cdot}h^{-1}{\cdot}g^{-1}$, with corresponding flow rates of CO_2, H_2, and N_2 being 24 mL/min, 72 mL/min, and 4 mL/min, respectively. N_2 was utilized as the internal standard gas. The resulting gas products were analyzed using an online gas chromatograph equipped with a TCD and a flame ionization detector (FID) (Agilent 7890A). Catalytic activity was measured every 6 h under each stable condition, producing three data sets per condition. The final value for each condition was determined by calculating the average and error of these data sets, which were then used to create charts.

CO_2 conversion (X_{CO_2}), methanol selectivity (S_{MeOH}), and space–time yield (STY_{MeOH}) are defined by the following three equations:

$$X_{CO_2}(\%) = \frac{n_{CO_{2,in}} - n_{CO_{2,out}}}{n_{CO_{2,in}}} \times 100\% \quad (3)$$

$$S_{MeOH}(\%) = \frac{n_{MeOH}}{n_{CO_{2,in}} - n_{CO_{2,out}}} \times 100\% \quad (4)$$

$$STY_{MeOH} = \frac{X_{CO_2} \times S_{MeOH} \times Flow_{CO_2} \times M_{MeOH}}{m_{cat}} \quad (5)$$

where $n_{CO_{2,in}}$ and $n_{CO_{2,out}}$ represent the molar number of CO_2 in and out before and after the reaction, n_{MeOH} represents the molar number of methanol in the product, $Flow_{CO_2}$ represents the flow of CO_2 during the reaction, M_{MeOH} represents the molar mass of methanol, m_{cat} represents the mass of the catalyst, respectively.

3. Results and discussion

3.1. Catalysts characterization

3.1.1. BET

The fundamental structural properties of the prepared perovskite catalysts, including specific surface area, pore volume, and pore size, were summarized in Table 1. All three catalysts exhibited low BET surface areas, a characteristic that is frequently observed in perovskite-type materials [17]. **Fig. S1** showed that the catalyst sample exhibited both microporous and smaller mesoporous structures. Meanwhile, LCZ-82 exhibited the smallest average pore size, predominantly featuring a microporous configuration. Additionally, LCZ-82 had a higher BET surface area than LC, indicating that Zn doping enhanced the specific surface area of Cu-based catalysts. The introduction of Mn through doping led to a reduction in the specific surface area of the catalyst, accompanied by an increase in the pore size. This observation indicated that Mn modified the spatial structure of the crystals, thereby affecting the specific surface area of the catalyst, which was consistent with findings reported in existing literature [24]. Furthermore, it suggested that doping with Mn and Zn altered the interactions within the catalyst system.

3.1.2. XRD

The X-ray diffraction patterns of both the calcinated and reduced catalysts were presented in Fig. 1. From Fig. 1(a), it was evident that La_2CuO_4, characterized by its perovskite structure, was present in all samples [25]. Doping with various elements induced distinct modifications in the catalysts. **Fig. S5** indicated that the La_2CuO_4 phases corresponding to the three catalysts are slightly different. The addition of Zn induced a transition in the La_2CuO_4 phase of LCZ-82 from its initial orthorhombic perovskite structure (JCPDS # 80-1481) to another orthorhombic perovskite structure (JCPDS # 82-2098). This transition led to lattice distortion and alterations in its unit cell parameters. Furthermore, the intensity of the diffraction peaks associated with the La_2CuO_4 catalyst increased, with higher diffraction intensity signifying a greater number of crystal planes [26]. With the addition of Mn, the La_2CuO_4 phase transitioned into a higher crystallinity orthorhombic

Table 1
Physical properties of perovskite-type catalysts.

Samples	S_{BET} (m^2/g)	V_{Pore} (cm^3/g)	D_{Pore} (nm)
LMCZ-181	6.9	0.033	19.4
LCZ-82	8.9	0.014	6.3
LC	5.6	0.028	19.6

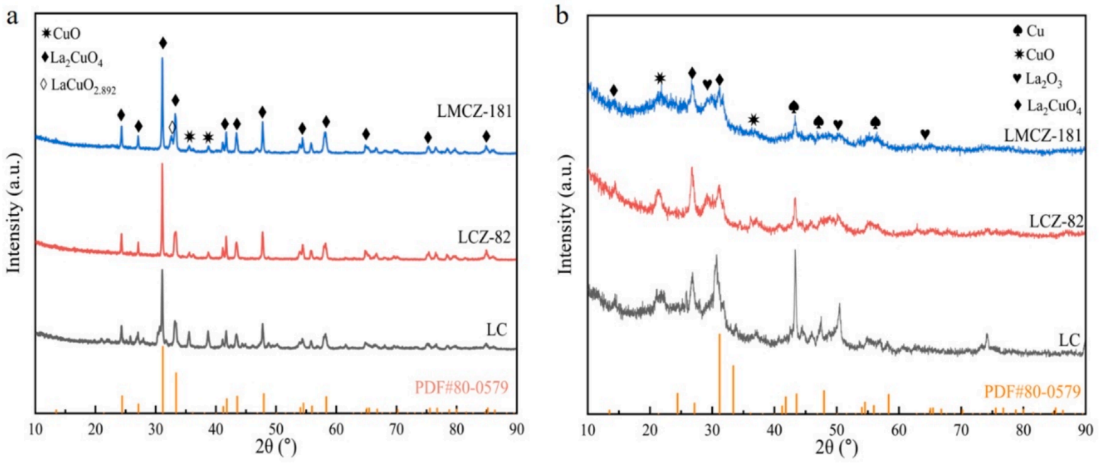

Fig. 1. XRD patterns of calcinated catalysts (a) and reduced catalysts (b).

perovskite structure (JCPDS # 80-0579), indicating that both Zn and Mn introductions led to alterations in the crystal structure of the catalyst. However, no new peaks were detected in the XRD patterns, and no novel phases containing Mn and Zn were observed in both LMCZ-181 and LCZ-82 samples. The absence of new phases may result from the low doping concentration and high dispersion of Mn and Zn. **Fig. S2** shows the XRD patterns of the catalyst after use, revealing that the catalyst's composition remained largely unchanged from its reduced state. The presence of Cu and La_2CuO_4 indicated that the catalysts exhibited good stability.

In the LMCZ-181 sample, a novel peak corresponding to $LaCuO_{2.892}$ (JCPDS # 79-1527) emerged at $2\theta = 32.9°$, indicating that the introduction of Mn led to structural defects in La_2CuO_4, consequently altering the oxygen vacancies. Furthermore, CuO (JCPDS # 80-0076) exhibited two diffraction peaks at $2\theta = 35.3°$ and 38.9° in all samples, suggesting the presence of Cu ions outside the perovskite structure [27]. A reduction in the perovskite structure of La_2CuO_4 was also observed in the reduced specimen. The detection of Cu and La_2O_3 indicated the partial reduction of La_2CuO_4, highlighting the effective dispersion of Cu within the perovskite-based catalysts [28].

The lattice parameters of the three catalysts were refined by the least squares method, with results summarized in Table 2. The incorporation of Zn induced elongation of the a-axis and expansion of the spatial structure of the catalyst, indicating that LCZ-82 contained a higher proportion of La_2CuO_4 than LC. This observation aligns with the enhanced diffraction peak intensity [24]. Following the Mn introduction, additional lattice parameter modifications were detected. Moreover, the average crystalline size of La_2CuO_4, calculated via Scherrer's equation, revealed a significant increase upon Mn and Zn incorporation.

3.1.3. SEM, TEM, and EDS energy spectra

As illustrated in Fig. 2(a–i), the synthesized perovskite catalysts exhibited granular crystalline structures. The LCZ-82 catalyst displayed enhanced crystallinity and uniform particle size distribution, consistent with a homogenous dispersion of La_2CuO_4 in the Zn-doped sample. In contrast, the Mn-doped LMCZ-181 catalyst exhibited rougher particle surfaces, resulting in a reduced average particle size and fragmented structures. This phenomenon is likely due to the partial replacement of Cu by Mn, leading to pore blockages [29]. The overall morphology of the catalysts showed minimal changes after use and reduction, indicating that the perovskite-type catalyst possesses strong anti-sintering properties. The XRD patterns indicated that Mn doping introduces structural defects in La_2CuO_4, accompanied by modifications in oxygen vacancies. Energy dispersion spectrometer (EDS) analysis of the LMCZ-181 confirmed the uniform distribution of La, Mn, Cu, Zn, and O on the catalyst surface. The uniform distribution of Cu implied that the active sites within the catalyst were evenly distributed, which was essential for the efficient progression of the catalytic reaction. Additionally, other literature on perovskite catalysts has also drawn similar conclusions that the distribution of active sites is relatively uniform [21,30].

Fig. 3 presents TEM images of the reduced catalysts, confirming the presence of La_2CuO_4 structures in all three catalysts. Notably, Fig. 3(b, d, and f) demonstrates that the LC-R and LCZ-82-R catalysts exhibit distinct lattice fringes corresponding to different crystal planes of CuO and La_2CuO_4, consistent with XRD findings. Among the catalysts, LMCZ-181 possessed a higher concentration of La_2CuO_4, which more effectively promoted the formation of small Cu particles. Moreover, based on the XRD and H_2-TPR results, the Cu species in the catalyst were selectively reduced during the calcination-reduction process. The larger Cu particles on the catalyst surface primarily formed through the reduction of CuO, adopting spherical structures. Meanwhile, the La_2O_3 phase was uniformly distributed on the catalyst surface alongside small Cu particles. Electron diffraction images displayed clear diffraction rings, indicating the high crystallinity of the various active metal species on the catalyst surface [30]. Fig. 3(g–l) illustrates the morphology and structure of the catalyst post-reaction, with the lattice structure remaining clearly visible. **Fig. S3** reveals that, even after 120 h of reaction, the metal components remained uniformly distributed on the catalyst surface, indicating the catalyst's excellent anti-sintering properties. Through the integration of XRD, SEM, TEM, and EDS energy spectra, it was deduced that the La-Mn-Cu-Zn catalyst consisted of closely associated La_2CuO_4 nanoparticles.

Table 2
The lattice parameters of the perovskite-type catalysts.

Samples	Lattice parameters of La_2CuO_4 (Å)			Volume (Å^3)	Size of La_2CuO_4 crystallites (nm)
	a	b	c		
LMCZ-181	5.371	5.396	13.164	381.6	41.6
LCZ-82	5.407	5.362	13.156	381.4	39.8
LC	5.379	5.361	13.156	380.5	28.0

3.1.4. H_2-TPR and H_2-TPD

The H_2-TPR profiles of the catalysts-R are depicted in Fig. 4(a). All samples exhibited reduction peaks corresponding to CuO and La_2CuO_4 within the temperature range of 190–300 °C, indicating that the reduction temperature of the perovskite catalyst is within 300 °C [31]. Particularly, the reduction peak of LC showed symmetrical characteristics, implying a relatively uniform distribution of Cu species in this catalyst. Additionally, this catalyst exhibited the largest reduction peak area due to its high content of Cu species. After the incorporation of Mn

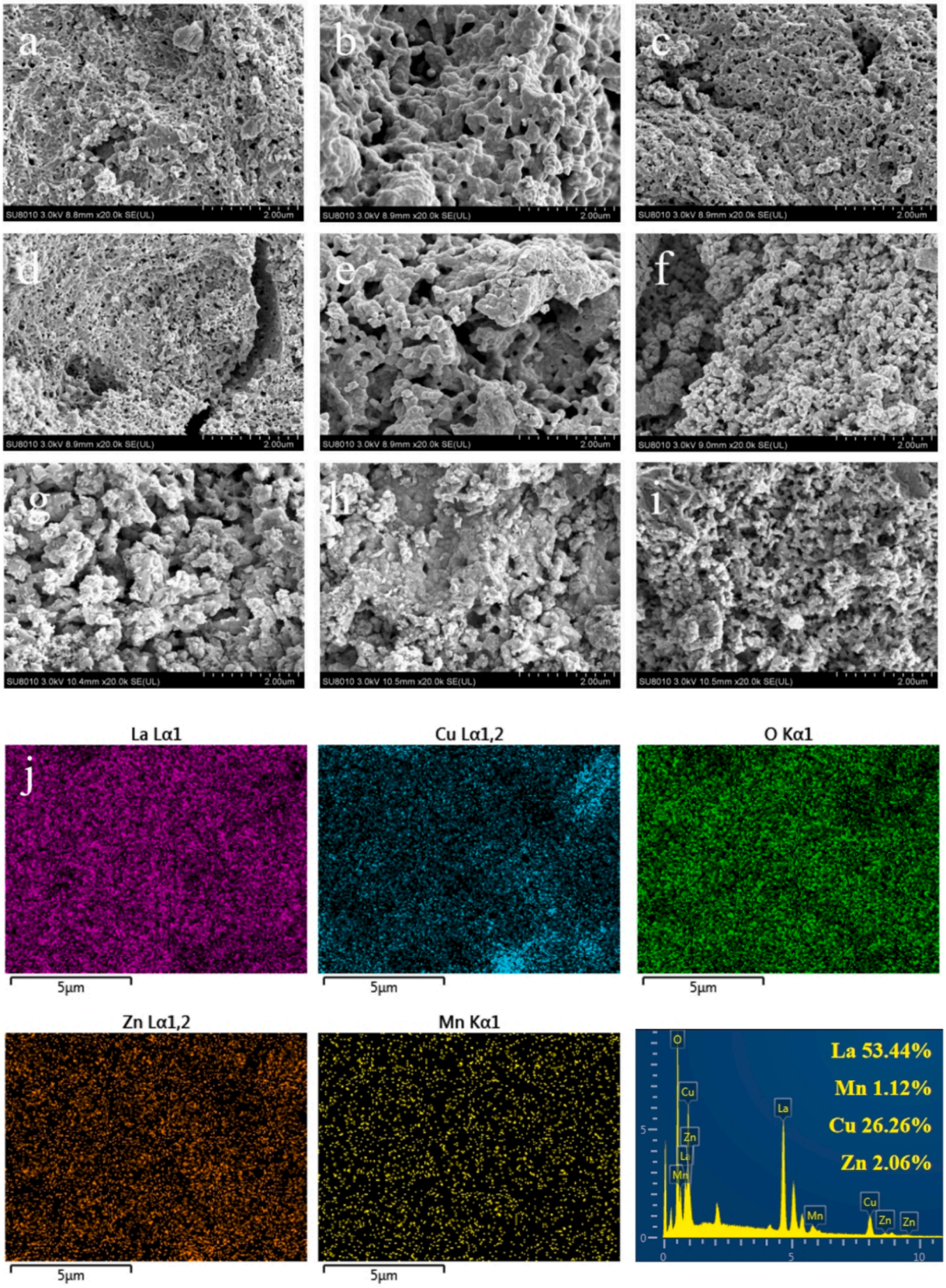

Fig. 2. SEM images of the perovskite catalysts: (a) LC-C; (b) LCZ-82-C; (c) LMCZ-181-C; (d) LC-R; (e) LCZ-82-R; (f) LMCZ-181-R; (g) LC-U; (h) LCZ-82-U; (i) LMCZ-181-U; (j) EDS energy spectra of LMCZ-181-R and surface scans of La, Mn, Cu, Zn, and O elements.

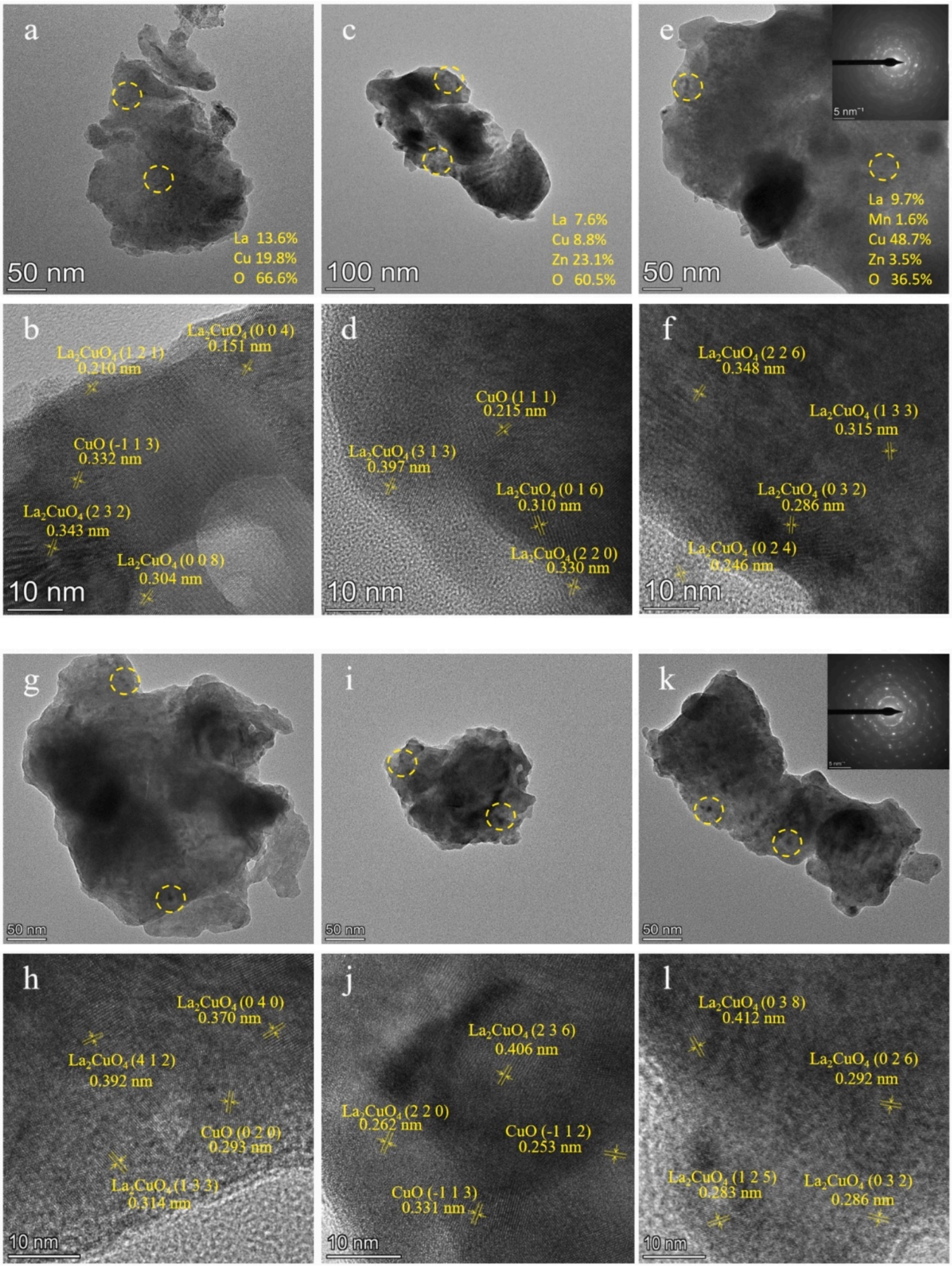

Fig. 3. TEM images of the perovskite catalysts: (a, b) LC-R; (c, d) LCZ-82-R; (e, f) LMCZ-181-R; (g, h) LC-U; (i, j) LCZ-82-U; (k, l) LMCZ-181-U.

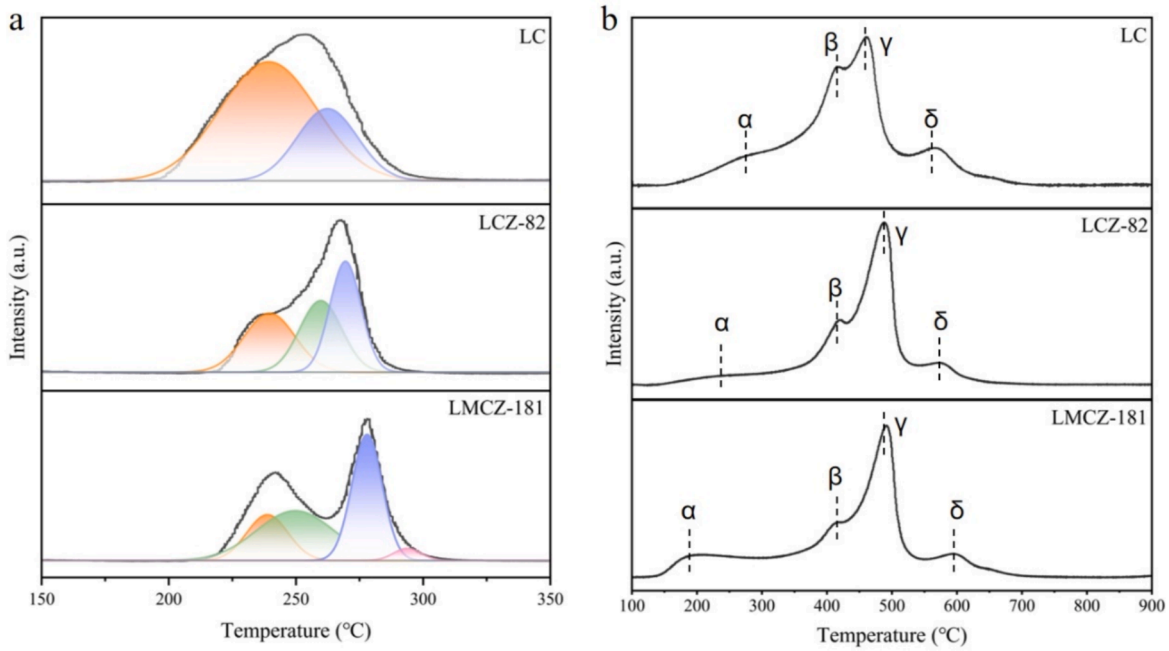

Fig. 4. (a) H_2-TPR and (b) H_2-TPD of the perovskite catalysts.

and Zn, the overall reduction temperature of the catalyst decreased. This suggested that doping with Mn and Zn significantly enhanced the reducibility of the samples. According to the literature, stronger metal-support interactions increase the difficulty of reduction while enhancing the dispersion of metal species on the catalyst surface. Both LCZ-82 and LMCZ-181 distinctly demonstrated that Cu species in these catalysts existed in two states: easily reducible (CuO) and difficult to reduce (La_2CuO_4). Moreover, the reduction peak width of LC is broader than those of LCZ-82 and LMCZ-181, likely due to its higher Cu content [32]. This resulted in an increased La_2CuO_4 crystal phase and larger microcrystal size, consistent with the lattice parameters obtained from XRD analysis.

The H_2-TPD profiles of the catalysts-R are presented in Fig. 4(b), with the corresponding H_2 adsorption data detailed in Table 3. Typically, H_2 adsorption and desorption at low temperatures are attributed to interactions with metal-active sites, while H_2 desorption peaks at higher temperatures are associated with hydrogen spillover on metal species. Notably, the capacity for H_2 adsorption and desorption at low-temperature conditions was particularly significant, given that the conventional reaction temperature for CO_2 hydrogenation to methanol typically ranged from 200 to 300 °C [33]. Compared to LC and LCZ-82, LMCZ-181 exhibited a shift in its H_2 desorption peak towards lower temperatures (150–300 °C) along with an increase in the amount of H_2 desorbed at this peak. This observation indicated an enhanced capacity for both H_2 adsorption and desorption. The enhanced low-temperature H_2 adsorption and desorption capacity facilitates more efficient CO_2 hydrogenation. The observed shift of the low-temperature desorption peak of H_2 shifting to earlier times aligned with the TPR results. This phenomenon may be attributed to a decrease in the reduction temperature of the catalyst, which consequently enhanced the availability of surface Cu active sites and increased the amount of adsorbed H_2. Furthermore, the high-temperature desorption peak of LMCZ-181 shifted to higher temperatures, suggesting that Mn doping promoted the generation of structural defects in the catalyst, leading to a more pronounced hydrogen spillover phenomenon. Both low- and high-temperature segments showed increased H_2 desorption upon Mn and Zn doping, indicating that the modified samples possess abundant Cu active sites, which promote efficient H_2 uptake and release [34].

3.1.5. *CO_2-TPD*

The temperature and peak area of CO_2 adsorption and desorption are indicative of the strength and number of basic sites on the catalyst surface [35]. As shown in Fig. 5, The CO_2-TPD curve can be separated into five peaks, namely peak α, peak β, peak γ, peak δ, and peak ε. Specifically, peak α represents a weak basic site (220–380 °C), while both peak β and peak γ indicate medium basic sites (380–550 °C). On the other hand, peak δ and peak ε correspond to strong basic sites (550–700 °C). Generally, peaks at higher temperatures signify strong basic sites with enhanced CO_2 adsorption capacity. Table 4 presents the CO_2 desorption temperatures as well as the adsorption capacity for each sample. It is observed that in the Zn-doped LCZ-82 catalyst, peaks α, β, and γ shift to higher temperatures, leading to a significant increase in the CO_2 adsorption capacity of weak and medium basic sites. This suggested that the catalyst's CO_2 adsorption performance was significantly improved. After the introduction of Mn, there was an overall increase in the CO_2 adsorption capacity of the catalyst, potentially due to the augmentation of pore volume and pore diameter. Compared to LCZ-82, LMCZ-181 exhibited significantly higher CO_2 adsorption at medium and strong basic sites. The enhanced CO_2 adsorption performance of the catalyst may be attributed to the trace $LaMnO_3$ structure, which

Table 3
H_2 desorption temperature and H_2 uptakes over the perovskite catalysts.

Samples	Temperature (°C)				H_2 uptake (μmol/g)				
	site α	site β	site γ	site δ	site α	site β	site γ	site δ	total
LC	260	435	460	563	100	152	185	74	511
LCZ-82	233	420	489	578	64	162	434	76	736
LMCZ-181	194	417	492	596	126	186	508	51	871

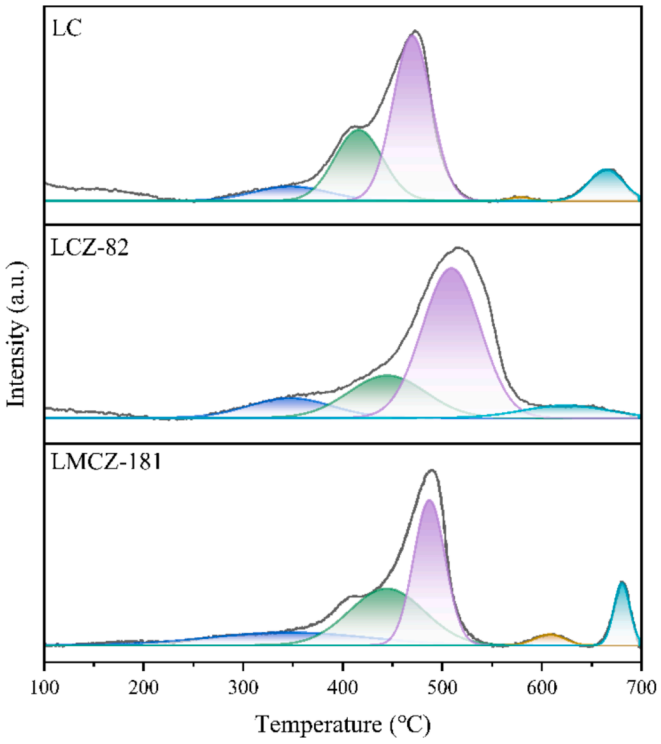

Fig. 5. CO_2-TPD of the perovskite catalysts.

strengthened the medium and the strong basic sites of the sample. The combined effect of Mn and Zn caused a collective shift of the basic sites in LMCZ-181 towards higher temperatures, resulting in an overall increase in the CO_2 adsorption capacity at each basic site. This indicated that LMCZ-181 may possess more oxygen vacancies, facilitating the adsorption of CO_2 on these vacancies or low coordination oxygen atoms, consequently enhancing the CO_2 adsorption performance at these basic sites. The reaction temperature for CO_2 hydrogenation to methanol ranges from 200 °C to 300 °C. Within this temperature range, LMCZ-181 exhibited peak α desorption at a lower temperature, accompanied by an increased CO_2 uptake capacity. This suggests that LMCZ-181 possesses the highest CO_2 adsorption capability, thereby enhancing the reaction process.

3.1.6. XPS

The XPS analysis of the catalyst-R revealed energy spectra of the Cu 2p orbitals for all three perovskite catalysts in Fig. 6(a). In LMCZ-181, two characteristic peaks were identified at binding energies of 932.29 eV and 952.06 eV, corresponding to Cu $2p_{3/2}$ and Cu $2p_{1/2}$ respectively. Notably, the peak for Cu $2p_{3/2}$ indicates both Cu^+ and Cu^{2+} species [36]; conversely, the peak for Cu $2p_{1/2}$ specifically corresponds to Cu^{2+}. This observation suggested that additional Cu species exist within the perovskite structure [37]. The Auger electron spectrum of Cu LMM in Fig. 6(b) shows a broad peak centered around a binding energy of approximately 917.18 eV, which was assigned to Cu^+ (916.7 eV) and Cu^0 (918.6 eV) [38]. The research indicated that Cu species in the catalyst predominantly exist in the Cu^0 form, alongside Cu^{2+} and Cu^+ forms [22]. Upon Mn doping, there was an increase in the broad peak at a binding energy of 917.5 eV, signifying an enhancement in Cu^0 and Cu^+ species within LMCZ-181. This finding implied that Mn-Cu interaction facilitated the Cu^{2+} reduction to Cu^+ and Cu^0. Additionally, two new peaks were observed in the reduced LC at approximately 911.05 eV and 914.5 eV, indicating the existence of $Cu^{\alpha+}$ (Cu species excluding Cu^{2+}, Cu^+, and Cu^0) within the perovskite system. Oxygen vacancies resulting from the oxygen deficiency in perovskite structures may induce abnormal oxidation states in transition metal ions (such as Cu), additionally, synergistic interactions between Cu and other elements (e.g. Mn, Zn) could also contribute to the formation of $Cu^{\alpha+}$ [24]. It was reported that the existence of $Cu^{\alpha+}$ played a pivotal role in the CO_2-to-methanol synthesis reaction [39]. $Cu^{\alpha+}$ facilitates the dissociation of H_2, thereby enhancing the hydrogenation of CO_2. Consequently, it serves effectively as the catalyst's active site. Compared to conventional Cu/Zn/Al catalysts, Cu-based perovskite catalysts exhibit unique valence states of Cu species, enriching the reactivity sites for the reaction.

The energy spectra of the La 3d orbitals for the three perovskite catalysts are depicted in Fig. 6(c). The binding energies of the three catalysts observed for La $3d_{5/2}$ are approximately 834.4 eV, close to the binding energy of La_2O_3, providing that all La ions exist in the trivalent form [40]. Following the introduction of Zn and Mn, there was a slight alteration in the binding energy of La $3d_{5/2}$, potentially attributed to variations in crystal structure and electronic configuration.

The energy spectra of the O 1s orbitals are depicted in Fig. 6(d). According to the fitting data, three characteristic peaks representing oxygen components are observed at binding energies of 528.61 eV, 530.55 eV, and 532.06 eV. The oxygen species observed at 528.61 eV are primarily O^{2-}, which can be attributed to the lattice oxygen ions. At 530.55 eV, the primary oxygen species is O^-, which corresponds to chemisorbed oxygen occupying oxygen vacancies or defects. At 532.06 eV, the notable oxygen species is O_2, associated with physically adsorbed oxygen on the surface [41]. Specifically, the signal at 528.61 eV represents lattice oxygen (O_{lat}) in perovskite-type catalysts, while those at 530.55 eV and 532.06 eV correspond to highly active adsorbed oxygen species (O_{ad}) associated with oxygen vacancies [42]. In general, adsorbed oxygen species (O_{ad}) play a crucial role in enhancing adsorption and desorption capabilities for CO_2 and H_2, thereby enhancing the overall reaction activity. Research has demonstrated that the ratio of O_{ad}/O_{lat} serves as an effective metric for characterizing the concentration of oxygen vacancies on the catalyst surface [43]. With the incorporation of Mn and Zn, there is a notable increase in the content of adsorbed oxygen (O_{ad}). LMCZ-181 exhibits the highest O_{ad}/O_{lat} ratio, suggesting that this perovskite catalyst more readily forms oxygen vacancies, thus enhancing their catalytic activity.

3.2. Catalytic tests

The catalytic performance of the three catalysts employed for CO_2 hydrogenation to methanol is illustrated in Fig. 7. As the temperature increased, the CO_2 conversion of each catalyst initially rose and then declined, while the methanol selectivity gradually decreased. Moreover, the overall trend of methanol yield exhibited an initial increase followed by a decrease. It should be noted that as an exothermic reaction, high temperatures are not conducive to the progress of CO_2 hydrogenation and methanol synthesis. Indeed, elevating the temperature was advantageous for the activation and conversion of CO_2 in the reaction.

Table 4
CO_2 desorption temperatures and CO_2 uptakes of the perovskite catalysts.

Samples	Temperature (℃)					CO_2 uptake (μmol/g)					
	site α	site β	site γ	site δ	site ε	site α	site β	site γ	site δ	site ε	total
LC	348	416	470	578	665	73	157	448	34	76	788
LCZ-82	347	445	509	540	624	105	176	470	—	47	798
LMCZ-181	346	444	487	608	680	105	123	646	38	88	1000

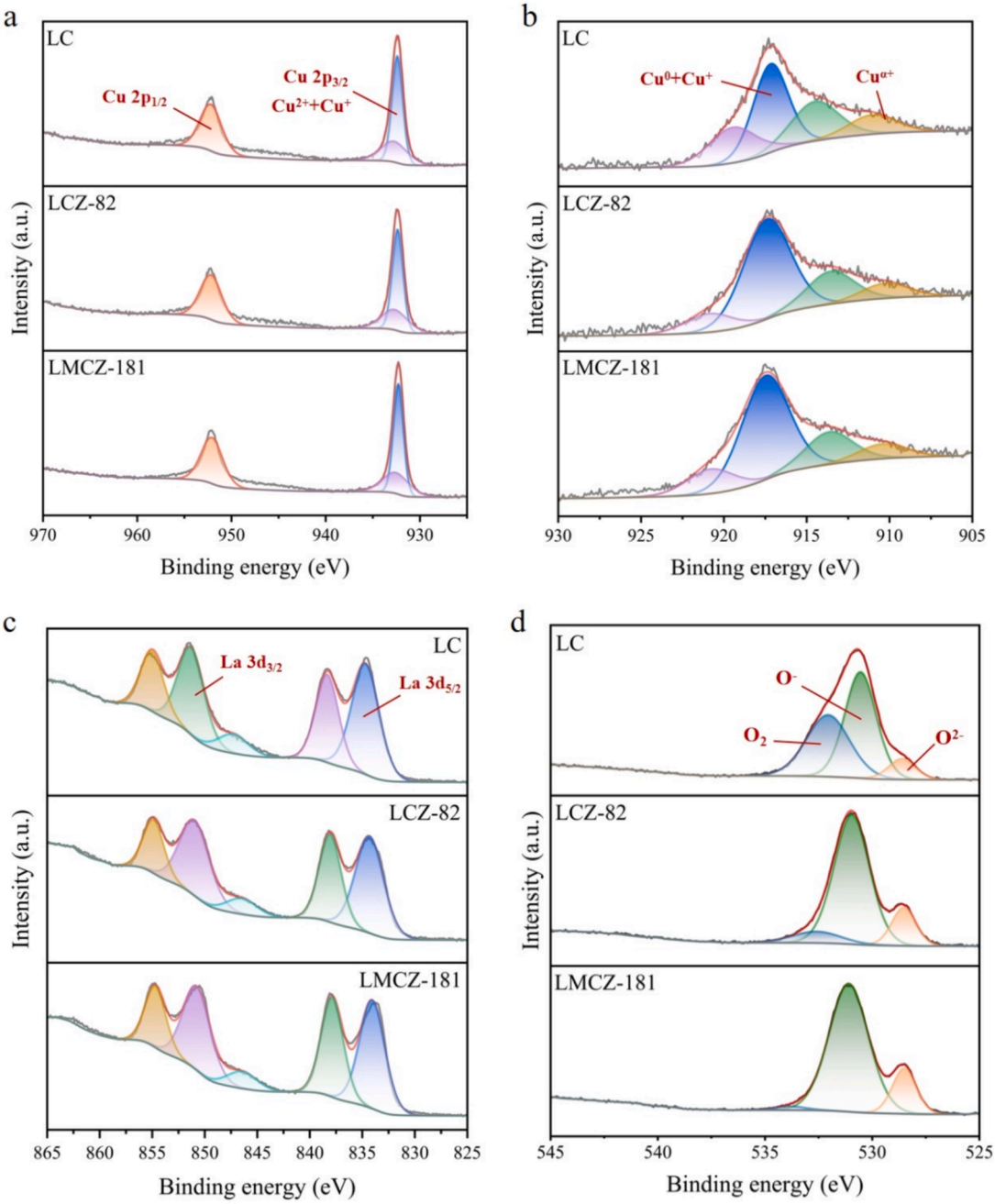

Fig. 6. XPS spectra of the perovskite catalysts: (a) Cu 2p; (b) Cu LMM Auger; (c) La 3d; (d) O 1s.

However, owing to the endothermic nature of the RWGS reaction and the higher apparent activation energy, the preferential formation of CO over methanol was favored; thus, an increase in temperature resulted in a decline in methanol selectivity. Importantly, Zn-doped LCZ-82 exhibited a remarkable enhancement in CO_2 conversion relative to LC and also mitigated the decline in methanol selectivity. After Mn doping, the CO_2 conversion of LMCZ-181 was further improved, while maintaining a consistent trend in methanol selectivity as observed in LCZ-82. Among the three catalysts, LMCZ-181 doped with Mn and Zn demonstrated superior catalytic performance, achieving the highest CO_2 conversion and methanol selectivity across all temperature ranges. Under the reaction conditions of 270 °C, 3 MPa, and GHSV = 6000 $mL{\cdot}h^{-1}{\cdot}g^{-1}$, LMCZ-181 displayed the most efficient catalytic activity with a CO_2 conversion of 20.81 %, methanol selectivity of 77.68 %, and methanol yield of 330.25 $mg_{MeOH}{\cdot}g_{cat}^{-1}{\cdot}h^{-1}$. These results highlighted the significant influence of Mn and Zn on both the physicochemical properties and performance of the catalyst.

Fig. 7(d) evaluates the catalyst stability of LMCZ-181 under the reaction conditions of 270 °C, 3 MPa, and GHSV = 6000 $mL{\cdot}h^{-1}{\cdot}g^{-1}$. As the reaction time extended from 6 h to 120 h, the CO_2 conversion on LMCZ-181 decreased from 20.9 % to 19.3 %, while the selectivity for methanol remained stable at approximately 77 %. These results indicated that the modified catalyst synthesized in this study exhibits excellent catalytic activity and stability.

This study conducted a comparison of the optimized LMCZ-181 catalyst against other Cu-based catalysts documented in recent literature, as presented in Table 5. The LMCZ-181 catalyst exhibited both a high CO_2 conversion rate and methanol selectivity concurrently, thereby demonstrating exceptional catalytic activity.

Based on the XRD results, it can be concluded that all samples

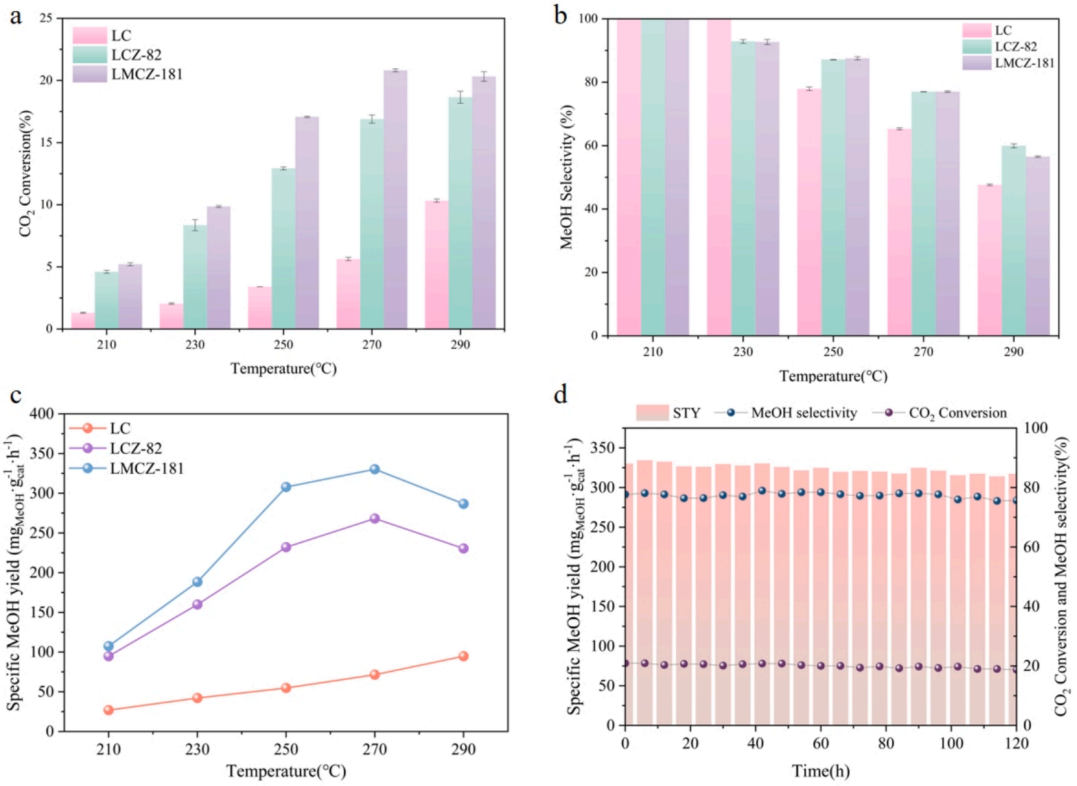

Fig. 7. The catalytic performance of the catalysts: (a) CO_2 conversion; (b) methanol selectivity; (c) methanol yield; (d) catalyst stability test.

Table 5
A comparison of the catalytic activity of LMCZ-181 catalyst with other Cu-based catalysts reported in recent literature studies.

Catalyst	P(MPa)	T(℃)	CO_2 conversion(%)	MeOH selectivity(%)	Ref
Cu/Zn/Al/Zr	4.0	240	18.7	47.2	[44]
Cu/ZnO/ZrO_2	5.0	270	23.0	56.8	[10]
Cu-ZnO/Al_2O_3-ZrO_2	5.0	280	23.1	38.0	[45]
CuZnAlZr	3.0	250	25.8	49.1	[46]
Cu-$ZnO^{MOF} \subset Al_2O_3$	3.0	240	9.1	86.9	[47]
Cu/ZnFe-0.5	4.5	260	9.4	71.6	[48]
LMCZ-181	3.0	270	20.8	77.6	this work

contain La_2CuO_4 with an orthorhombic perovskite structure, as shown in Fig. 8. Combined with the characterization results of H_2-TPD and CO_2-TPD, Zn could effectively increase the medium-basic sites of the catalysts to establish a Cu-O-Zn interface. This interface facilitated the adsorption of H_2 and CO_2 on the catalyst, thereby improving the efficiency of the catalytic reaction [49–51]. Mn facilitated the production of more structural defects and oxygen vacancies in the catalyst, allowing more H_2 and CO_2 to be adsorbed on the oxygen vacancies or low-coordinated oxygen atoms. The superior reactivity of LMCZ-181 at 270 °C could be attributed to the adsorption and activation of CO_2 on the medium-basic sites. Typically, Cu species are essential in the action process of each catalyst [35]. According to CO_2-TPD, it can be concluded that LMCZ-181 has the highest number of surface basic sites. Li et al. [10] prepared a series of Cu/Zn/ZrO_2 catalysts with different $NaBH_4$ content reduced by the precipitation-reduction method for methanol synthesis from CO_2 hydrogenation, drawing conclusions related to methanol selectivity and the distribution of surface basic centers. In this study, the number of basic sites was quantified based on the CO_2 adsorption on the medium-basic sites, and an increase in the number of basic sites resulted in enhanced methanol selectivity. Furthermore, it was observed from H_2-TPR analysis and EDS energy spectrum that the higher Cu content in the LC did not lead to increased CO_2 conversion, suggesting that the CO_2 conversion depended not only on Cu content but

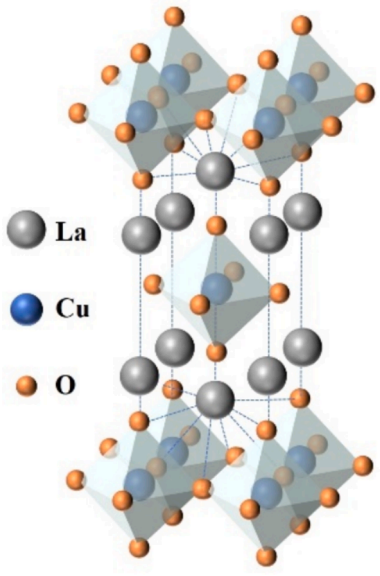

Fig. 8. Orthorhombic perovskite structure of La_2CuO_4.

also on active sites and interfaces on the catalyst surface. In LMCZ-181, the oxygen vacancies generated from the oxygen deficiency led to a unique oxidation state $Cu^{\alpha+}$, increasing the active sites of the reaction. Despite having a lower Cu content compared to LC, LMCZ-181 exhibited an increased abundance of special valence states for Cu species and a higher concentration of oxygen vacancies, resulting in significantly improved catalytic activity.

It is well known that Cu served as the active phase for the hydrogenation of CO_2 to methanol on Cu-based catalysts [4]. According to CO_2-TPD, Zn amplified adsorption and activation processes for CO_2, significantly influencing the distribution of Cu active sites. Importantly, methanol selectivity is related to the number of medium basic sites; an increase in these sites corresponds with higher selectivity. Both Mn and Zn doping significantly enhance these sites, with LMCZ-181 presenting exceptional selectivity and yield for methanol. Prior research demonstrated that ZnO functioned as both a support material and a promoter. The interface between ZnO and Cu is critical for providing active sites necessary for methanol production [23,52]. Furthermore, Cu supported on such substrates exhibited increased catalytic activity due to stronger interactions with the support material [53]. H_2-TPR profiles also demonstrated that Mn and Zn doping heighten sample reducibility, implying stronger metal-support interactions and enhanced metal dispersion on the catalyst surface.

3.3. Possible reaction mechanism

Fig. 9(a–c) shows the in-situ DRIFTS spectra for CO_2 hydrogenation over LC, LCZ-82, and LMCZ-181 catalysts. The absorption peaks observed at 1083 cm^{-1} and 1149 cm^{-1} corresponded to CH_3O* species, while those at 1339 cm^{-1} were attributed to HCO_3* species. Peaks at 1383 cm^{-1} and 1558 cm^{-1} corresponded to HCOO* species, and those at 1437 cm^{-1} and 1484 cm^{-1} were associated with CO_3* species. Therefore, CO_3*, HCO_3*, and HCOO* species are identified as the primary reaction intermediates in the hydrogenation of CO_2 to methanol. Weak signals for the by-product CO were detected at 2078 cm^{-1} and 2108 cm^{-1}. Although the reaction intermediates were similar across the three catalysts, the peak intensities of CO_3*, HCO_3*, and HCOO* for LMCZ-181 were significantly higher than those of the other catalysts. At 270 °C, the absorption peak of HCOO* species at 1558 cm^{-1} was selected for detailed analysis. Over time, the HCOO* species' absorption peak for LMCZ-181 exhibited a continuous increase. It was significantly higher than that of the other catalysts, resulting in enhanced conversion of CH_3O* species and the highest yield of CH_3OH. This suggests that LMCZ-181 demonstrates superior CO_2 and H_2 adsorption and activation, facilitating the formation of reaction intermediates. This observation aligns with findings obtained from CO_2-TPD and H_2-TPR experiments. Furthermore, for HCOO* species, LCZ-82 reached a stable state faster than LC, suggesting that LCZ-82 has a higher catalytic reaction rate and enhanced hydrogenation capability compared to LC.

To further elucidate the mechanism of CO_2 hydrogenation and

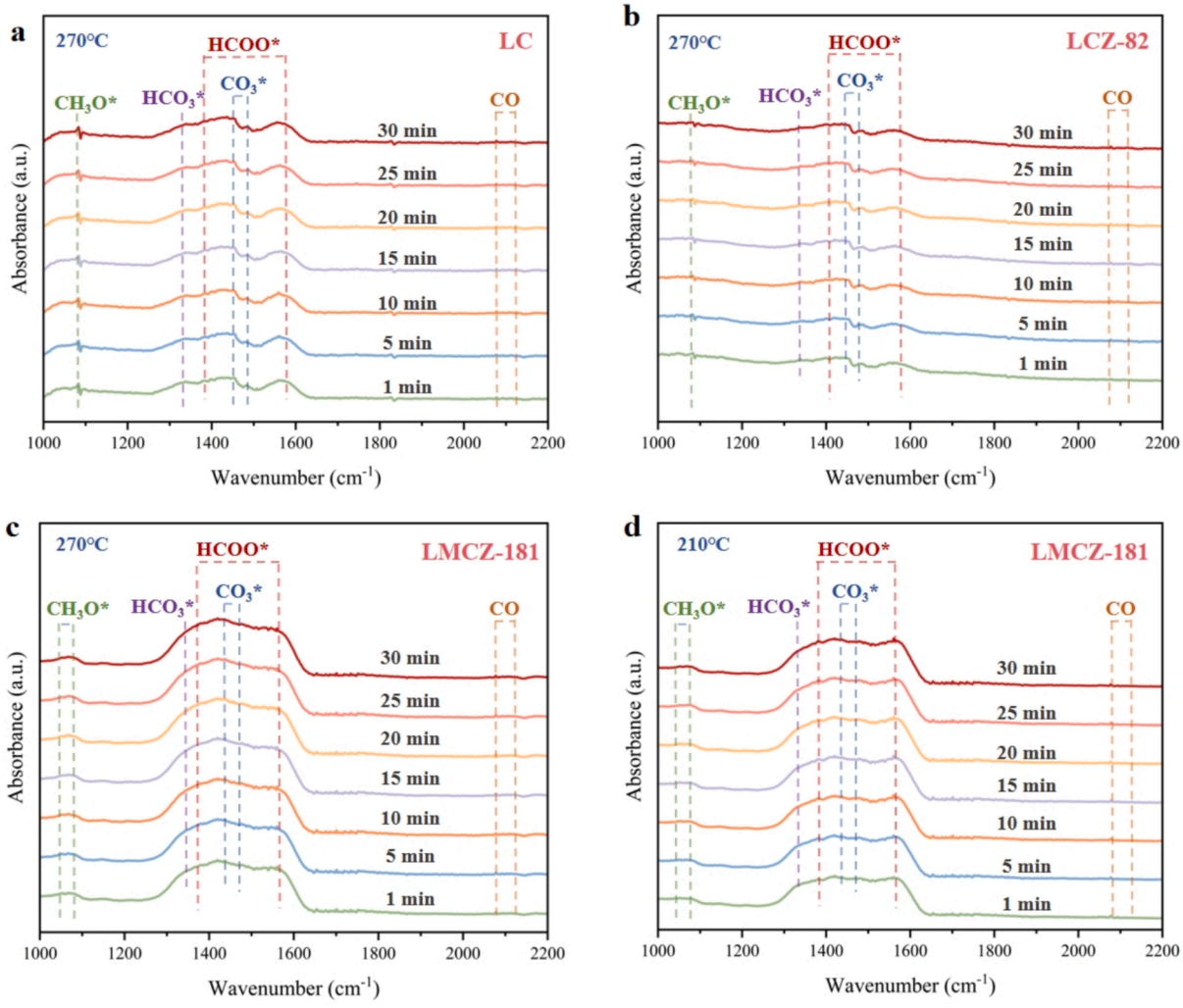

Fig. 9. In-situ DRIFT spectra of catalysts: (a) LC; (b) LCZ-82; (c, d) LMCZ-181.

methanol synthesis, CO_2 and H_2 were introduced at 210 °C and 270 °C to examine the reaction intermediates involved in CO_2 hydrogenation to methanol, as shown in Fig. 9(d). CH_3O* species were derived from the conversion of HCOO* species. At 210 °C on LMCZ-181, the concentration of CH_3O* species is relatively low, while HCOO* species accumulate significantly, indicating that the latter may represent the rate-limiting step [54]. As the temperature increases from 210 °C to 270 °C, the absorption peak intensity of CH_3O* increases, suggesting enhanced formation of key intermediates at higher temperatures. Additionally, CO_2 hydrogenation on Cu-based catalysts typically proceed via two pathways: the formate and the carboxyl pathway. In the formate pathway, formate serves as a common intermediate for methanol synthesis [55]. Activated CO_2 is converted into formate (HCOO*), which is then hydrogenated into methoxy (CH_3O*) and methanol [56]. In the carboxyl pathway, adsorbed CO_2 is transformed into CO* through sequential hydrogenation reactions and further hydrogenated into intermediates such as HCOO*, H_2COO*, HCO*, and H_2CO*, which are either converted into methanol or directly desorbed from the surface [57]. This study detected HCOO* and CH_3O* species across all three catalysts, confirming the existence of an HCOO*-CH_3O*-CH_3OH* pathway in the CO_2 hydrogenation process and highlighting the significance of the formate pathway on Cu-based catalysts.

4. Conclusions

A series of La-Mn-Cu-Zn-O catalysts, derived from perovskite-type precursors, were synthesized using the citrate complexation method for CO_2 hydrogenation to methanol. The results indicated that all the catalysts exhibited a La_2CuO_4 perovskite structure. Under the conditions of 270 °C, 3 MPa, and GHSV = 6000 $mL{\cdot}h^{-1}{\cdot}g^{-1}$, LMCZ-181 exhibited superior catalytic activity and stability, achieving CO_2 conversion and methanol selectivity of 20.81 % and 77.68 %, respectively. Catalysts modified with Mn and Zn demonstrated optimal catalytic performance due to the alterations in the crystal structure, which increased oxygen vacancies and promoted the formation of active sites, thereby enhancing hydrogenation efficiency. Importantly, the incorporation of Mn increased in Cu^0 and Cu^+ species and facilitated the formation of distinct valence states of Cu species $Cu^{\alpha+}$ ($0 < \alpha < 1$), which played a crucial role in CO_2 conversion to methanol. In-situ DRIFTS results suggested that these catalysts achieve CO_2 hydrogenation via the formate pathway and confirmed the enhanced hydrogenation capabilities of LMCZ-181. This study provides new insights into the structural modulation of Cu-based catalysts.

CRediT authorship contribution statement

Yuxin Shi: Writing – review & editing, Writing – original draft, Methodology, Investigation, Data curation. **Lingjun Zhu:** Writing – review & editing, Supervision, Funding acquisition, Data curation, Conceptualization. **Jiaqi Tang:** Investigation, Data curation. **Kunzan Qiu:** Writing – review & editing, Supervision. **Shurong Wang:** Writing – review & editing, Supervision, Project administration, Funding acquisition, Conceptualization.

Declaration of competing interest

The authors declare that they have no known competing financial interests or personal relationships that could have appeared to influence the work reported in this paper.

Acknowledgments

The authors are grateful for the financial support provided by Zhejiang Provincial Natural Science Foundation of China (LDT23E06014E06), Zhejiang Provincial Basic Public Welfare Research Project (LGG22E060013) and the Fundamental Research Funds for the Central Universities (2022ZFJH04).

Appendix A. Supplementary data

Supplementary data to this article can be found online at https://doi.org/10.1016/j.fuel.2025.134931.

Data availability

Data will be made available on request.

References

[1] Fankhauser S, Smith SM, Allen M, Axelsson K, Hale T, Hepburn C, et al. The meaning of net zero and how to get it right. Nat Clim Chang 2022;12:15–21.
[2] Tapia JFD, Lee J-Y, Ooi REH, Foo DCY, Tan RR. A review of optimization and decision-making models for the planning of CO_2 capture, utilization and storage (CCUS) systems. Sustain Prod Consump 2018;13:1–15.
[3] Biswal T, Shadangi KP, Sarangi PK, Srivastava RK. Conversion of carbon dioxide to methanol: a comprehensive review. Chemosphere 2022;298:134299.
[4] Dang S, Yang H, Gao P, Wang H, Li X, Wei W, et al. A review of research progress on heterogeneous catalysts for methanol synthesis from carbon dioxide hydrogenation. Catal Today 2019;330:61–75.
[5] Zhang C, Yang H, Gao P, Zhu H, Zhong L, Wang H, et al. Preparation and CO_2 hydrogenation catalytic properties of alumina microsphere supported Cu-based catalyst by deposition-precipitation method. J CO_2 Util 2017;17:263–72.
[6] Rodriguez JA, Liu P, Stacchiola DJ, Senanayake SD, White MG, Chen JG. Hydrogenation of CO_2 to methanol: importance of metal–oxide and metal–carbide interfaces in the activation of CO_2. ACS Catal 2015;5:6696–706.
[7] Li K, Chen JG. CO_2 hydrogenation to methanol over ZrO_2-containing catalysts: insights into ZrO_2 induced synergy. ACS Catal 2019;9:7840–61.
[8] Arena F, Italiano G, Barbera K, Bonura G, Spadaro L, Frusteri F. Basic evidences for methanol-synthesis catalyst design. Catal Today 2009;143:80–5.
[9] Kattel S, Ramírez PJ, Chen JG, Rodriguez JA, Liu P. Active sites for CO_2 hydrogenation to methanol on Cu/ZnO catalysts. Science 2017;355:1296–9.
[10] Dong X, Li F, Zhao N, Xiao F, Wang J, Tan Y. CO_2 hydrogenation to methanol over Cu/ZnO/ZrO_2 catalysts prepared by precipitation-reduction method. Appl Catal B: Environ 2016;191:8–17.
[11] Wu C, Lin L, Liu J, Zhang J, Zhang F, Zhou T, et al. Inverse ZrO_2/Cu as a highly efficient methanol synthesis catalyst from CO_2 hydrogenation. Nat Commun 2020;11:5767.
[12] Guo X, Mao D, Lu G, Wang S, Wu G. The influence of La doping on the catalytic behavior of Cu/ZrO_2 for methanol synthesis from CO_2 hydrogenation. J Mol Catal A Chem 2011;345:60–8.
[13] Yao L, Shen X, Pan Y, Peng Z. Synergy between active sites of Cu-In-Zr-O catalyst in CO_2 hydrogenation to methanol. J Catal 2019;372:74–85.
[14] Sun XF, Komiya S, Ando Y. Anomalous damping of phonon thermal transport in lightly Y- or Eu-doped La_2CuO_4 single crystals. Physica C 2003;388–389:355–6.
[15] Chakraborty T, Ray S. Evolution of diffuse microscopic phases and magnetism in Ca, Fe co-doped $BaTiO_3$. J Alloys Compd 2014;610:271–5.
[16] Jia L, Gao J, Fang W, Li Q. Carbon dioxide hydrogenation to methanol over the pre-reduced $LaCr_{0.5}Cu_{0.5}O_3$ catalyst. Catal Commun 2009;10:2000–3.
[17] Peña MA, Fierro JLG. Chemical structures and performance of perovskite oxides. Chem Rev 2001;101:1981–2018.
[18] Jia L, Gao J, Fang W, Li Q. Influence of copper content on structural features and performance of pre-reduced $LaMn_{1-x}Cu_xO_3$ ($0 \le x < 1$) catalysts for methanol synthesis from CO_2/H_2. J Rare Earths 2010;28:747–51.
[19] Maluf SS, Assaf EM. Effects of the partial replacement of La by M (M=Ce, Ca and Sr) in $La_{2-x}M_xCuO_4$ perovskites on catalysis of the water-gas shift reaction. J Nat Gas Chem 2010;19:567–74.
[20] Zhang Y, Guo S, Tian Z, Zhao Y, Hao Y. Experimental investigation of steam reforming of methanol over La_2CuO_4/CuZnAl-oxides nanocatalysts. Appl Energy 2019;254:113022.
[21] Xaba BS, Friedrich HB, Singh S, Mahomed AS. The influence of La incorporation on the performance of the $Cu_xCe_yLa_{1-(x+y)}O_{2-\delta}$ catalysts for CO_2 hydrogenation to methanol. Mol Catal 2024;567:114476.
[22] Zhan H, Li F, Gao P, Zhao N, Xiao F, Wei W, et al. Methanol synthesis from CO_2 hydrogenation over La–M–Cu–Zn–O (M = Y, Ce, Mg, Zr) catalysts derived from perovskite-type precursors. J Power Sources 2014;251:113–21.
[23] Cui W-G, Li Y-T, Yu L, Zhang H, Hu T-L. Zeolite-encapsulated ultrasmall Cu/ZnO_x nanoparticles for the hydrogenation of CO_2 to methanol. ACS Appl Mater Interfaces 2021;13:18693–703.
[24] Zhan H, Li F, Xin C, Zhao N, Xiao F, Wei W, et al. Performance of the La–Mn–Zn–Cu–O based perovskite precursors for methanol synthesis from CO_2 hydrogenation. Catal Lett 2015;145:1177–85.
[25] Ma W, Zhang S, Deng L, Zhong D, Li K, Liu X, et al. Cu-based perovskite as a novel CWPO catalyst for petroleum refining wastewater treatment: performance, toxicity and mechanism. J Hazard Mater 2023;448:130824.
[26] Wang X, Zhu L, Zhuo Y, Zhu Y, Wang S. Enhancement of CO_2 methanation over La-modified Ni/SBA-15 catalysts prepared by different doping methods. ACS Sustainable Chem Eng 2019;7:14647–60.

[27] Porta P, De Rossi S, Faticanti M, Minelli G, Pettiti I, Lisi L, et al. Perovskite-type oxides. J Solid State Chem 1999;146:291–304.
[28] Zhang Z, Chen X, Zhang X, Lin H, Lin H, Zhou Y, et al. Synthesis of Cu_2O/La_2CuO_4 nanocomposite as an effective heterostructure photocatalyst for H_2 production. Catal Commun 2013;36:20–4.
[29] Li F, Dong X, Zhao N, Xiao F. Influence of $NaBH_4$ liquid reduction over LaCuZn perovskite for CO_2 hydrogenation to methanol. Catal Lett 2020;150:922–9.
[30] Feng C, Gao Q, Xiong G, Chen Y, Pan Y, Fei Z, et al. Defect engineering technique for the fabrication of $LaCoO_3$ perovskite catalyst via urea treatment for total oxidation of propane. Appl Catal B: Environ 2022;304:121005.
[31] Natesakhawat S, Ohodnicki PR, Howard BH, Lekse JW, Baltrus JP, Matranga C. Adsorption and deactivation characteristics of Cu/ZnO-based catalysts for methanol synthesis from carbon dioxide. Top Catal 2013;56:1752–63.
[32] Guo X, Mao D, Lu G, Wang S, Wu G. Glycine–nitrate combustion synthesis of CuO–ZnO–ZrO_2 catalysts for methanol synthesis from CO_2 hydrogenation. J Catal 2010;271:178–85.
[33] Gao P, Li F, Xiao F, Zhao N, Sun N, Wei W, et al. Preparation and activity of Cu/Zn/Al/Zr catalysts via hydrotalcite-containing precursors for methanol synthesis from CO_2 hydrogenation. Catal Sci Technol 2012;2:1447.
[34] Zhang L, Zhang Y, Chen S. Effect of promoter SiO_2, TiO_2 or SiO_2-TiO_2 on the performance of CuO-ZnO-Al_2O_3 catalyst for methanol synthesis from CO_2 hydrogenation. Appl Catal A 2012;415–416:118–23.
[35] Li F, Zhan H, Zhao N, Xiao F. CO_2 hydrogenation to methanol over La-Mn-Cu-Zn-O based catalysts derived from perovskite precursors. Int J Hydrogen Energy 2017;42:20649–57.
[36] Zhu J, Wang Y, Zhi A, Chen Z, Shi L, Zhang Z, et al. Cation-deficiency-dependent CO_2 electroreduction over copper-based Ruddlesden–Popper perovskite oxides. Angew Chem Int Ed 2022;61:e202111670.
[37] Liu J, Han C, Yang X, Gao G, Shi Q, Tong M, et al. Methyl formate synthesis from methanol on titania supported copper catalyst under UV irradiation at ambient condition: performance and mechanism. J Catal 2016;333:162–70.
[38] Li Z, Meng M, Zha Y, Dai F, Hu T, Xie Y, et al. Highly efficient multifunctional dually-substituted perovskite catalysts $La_{1-x}K_xCo_{1-y}Cu_yO_{3-\delta}$ used for soot combustion, NO_x storage and simultaneous NO_x-soot removal. Appl Catal B: Environ 2012;121–122:65–74.
[39] Arena F, Italiano G, Barbera K, Bordiga S, Bonura G, Spadaro L, et al. Solid-state interactions, adsorption sites and functionality of Cu-ZnO/ZrO_2 catalysts in the CO_2 hydrogenation to CH_3OH. Appl Catal A 2008;350:16–23.
[40] Maluf SS, Nascente PAP, Afonso CRM, Assaf EM. Study of $La_{2-x}Ca_xCuO_4$ perovskites for the low temperature water gas shift reaction. Appl Catal A 2012;413–414:85–93.
[41] Hernández WY, Tsampas MN, Zhao C, Boreave A, Bosselet F, Vernoux P. La/Sr-based perovskites as soot oxidation catalysts for Gasoline Particulate Filters. Catal Today 2015;258:525–34.
[42] Hu Y, Tao B, Shang F, Zhou M, Hao D, Fan R, et al. Thermal decomposition of ammonium perchlorate over perovskite catalysts: catalytic decomposition behavior, mechanism and application. Appl Surf Sci 2020;513:145849.
[43] Zhang X, Pei C, Chang X, Chen S, Liu R, Zhao Z-J, et al. FeO_6 octahedral distortion activates lattice oxygen in perovskite ferrite for methane partial oxidation coupled with CO_2 splitting. J Am Chem Soc 2020;142:11540–9.
[44] An X, Li J, Zuo Y, Zhang Q, Wang D, Wang J. A Cu/Zn/Al/Zr fibrous catalyst that is an improved CO_2 hydrogenation to methanol catalyst. Catal Lett 2007;118:264–9.
[45] Guo Q, Li S, Li J, Hu Y, Duanmu C. Enhanced CO_2 hydrogenation to methanol on the mesostructured Cu–ZnO/Al_2O_3–ZrO_2 catalyst. ACS Appl Energy Mater 2021;4:8311–21.
[46] Hou X-X, Xu C-H, Liu Y-L, Li J-J, Hu X-D, Liu J, et al. Improved methanol synthesis from CO_2 hydrogenation over CuZnAlZr catalysts with precursor pre-activation by formaldehyde. J Catal 2019;379:147–53.
[47] Qi T, Zhao Y, Chen S, Li W, Guo X, Zhang Y, et al. Bimetallic metal organic framework-templated synthesis of a Cu-ZnO/Al_2O_3 catalyst with superior methanol selectivity for CO_2 hydrogenation. Mol Catal 2021;514:111870.
[48] Liu T, Xu D, Wu D, Liu G, Hong X. Spinel $ZnFe_2O_4$ Regulates Copper Sites for CO_2 Hydrogenation to Methanol. ACS Sustainable Chem Eng 2021;9:4033–41.
[49] Miller BJA, Martin-luengo MA, Vong MSW, Wang Y, Self VA, Chapman SM, et al. Junctions between CuO_x and ZnO_y in sensors for CO and catalysts for CO hydrogenation. J Mater Chem 1997;7:2155–60.
[50] Choi Y, Futagami K, Fujitani T, Nakamura J. The role of ZnO in Cu/ZnO methanol synthesis catalysts—morphology effect or active site model? Appl Catal A 2001;208:163–7.
[51] Fujita S, Kanamori Y, Satriyo AM, Takezawa N. Methanol synthesis from CO_2 over Cu/ZnO catalysts prepared from various coprecipitated precursors. Catal Today 1998;45:241–4.
[52] Cui X, Yan W, Yang H, Shi Y, Xue Y, Zhang H, et al. Preserving the active Cu–ZnO interface for selective hydrogenation of CO_2 to dimethyl ether and methanol. ACS Sustainable Chem Eng 2021;9:2661–72.
[53] Ouyang B, Tan W, Liu B. Morphology effect of nanostructure ceria on the Cu/CeO_2 catalysts for synthesis of methanol from CO_2 hydrogenation. Catal Commun 2017;95:36–9.
[54] Cao M, Chen Y, Liu B, Zhang Z. CO_2 hydrogenation to methanol on efficient Pd modified α-MoC1−x catalysts. Fuel 2024;375:132587.
[55] Li H, Fang W, Wang L-X, Liu Y, Liu L, Sun T, et al. Physical regulation of copper catalyst with a hydrophobic promoter for enhancing CO_2 hydrogenation to methanol. Innovation 2023;4:100445.
[56] Mao D, Zhang H, Zhang J, Wu D. The influence of the compositions and structures of Cu-ZrO_2 catalysts on the catalytic performance of CO_2 hydrogenation to CH_3OH. Chem Eng J 2023;471:144605.
[57] Grabow LC, Mavrikakis M. Mechanism of methanol synthesis on Cu through CO_2 and CO hydrogenation. ACS Catal 2011;1:365–84.